



Improving real-time GNSS orbits and clocks by filtered integrated processing multiple LEO onboard and ground observations

Hongjie Zheng¹ · Yongqiang Yuan¹ · Xingxing Li¹ · Keke Zhang¹

Received: 3 November 2024 / Accepted: 8 April 2025

© The Author(s), under exclusive licence to Springer-Verlag GmbH Germany, part of Springer Nature 2025

Abstract

The real-time service (RTS) of providing precise satellite orbits and clocks is an important infrastructure for Global Navigation Satellite System (GNSS) precise positioning technologies. Filter-based precise orbit determination (POD) has been the promising trend in RTS for its superiority in terms of precision and stability. However, the heavy computational requirements and longer (re-)convergence time of filter-based POD limit its availability in some time-sensitive scenarios. In this study, we proposed a real-time integrated processing model to improve the performance of GNSS real-time orbits and clocks. Similar to the framework of filter-based POD, the proposed model integrates ground and LEO-onboard observations with square root information filter (SRIF). We collected real GNSS observation from eight LEO satellites to validate the proposed model. The results show that, by introducing onboard observations from eight LEO satellites, the convergence time, 3D RMS of GPS orbits and STD of GPS clocks can be improved by 30.4%, 46.9% and 37.5%, respectively, when using 30 globally distributed stations. When using the proposed model with ambiguity resolution (AR), the average 3D RMS of GPS orbits are 4.0 cm, which is improved by 27.8% compared to ground-only AR solutions. This accuracy is comparable to ground-only AR solutions with 90 stations, while improving computational efficiency by 66%. By using real-time products based on the proposed model, the positioning accuracy of GPS real-time kinematic PPP solutions can be improved by 27.7%, 30.9% and 28.5% in the east, north and up components, respectively, compared to that based on ground-only solutions with close computational performance.

Keywords GNSS real-time orbit and clock · LEO onboard observation · Integrated precise orbit determination · Ambiguity resolution · Square root information filter

Introduction

In recent years, real-time precise point positioning (PPP) and its extension, PPP-RTK (network-based real-time kinematic precise point positioning), have become key technologies for achieving centimeter-level positioning accuracy using single-receiver Global Navigation Satellite System (GNSS) measurements. These technologies rely on the availability of real-time precise GNSS orbits and clocks. Typically, real-time orbits are derived from the predicted components of ultra-rapid orbits, which are based on post-processed solutions (Li et al. 2019a). Given the challenges of accurately modeling satellite clock variations, filter-based precise clock

estimation is commonly employed to generate high-accuracy real-time clocks. It is important to note that the precision of real-time clock products using this approach depends heavily on the accuracy of the predicted orbits. Meanwhile, the inherent characteristics of predicted orbits cause their accuracy to decline rapidly as extrapolation time increases, particularly when using an imperfect solar radiation pressure (SRP) model, as well as during eclipse seasons and satellite maneuvering periods.

To address this limitation, filter-based real-time precise orbit determination (POD) has emerged as a promising approach. Unlike traditional method based on predicted orbits, this method utilizes real-time GNSS observation data to generate real-time orbits. Additionally, the satellite orbit dynamic model can be flexibly adjusted during abnormal operation periods, leading to more stable orbits (Dai et al. 2019). Moreover, since satellite clock parameters are also estimated within the filter-based POD, real-time clocks can

✉ Yongqiang Yuan
yqyuan@whu.edu.cn

¹ School of Geodesy and Geomatics, Hubei Luojia Laboratory, Wuhan University, 129 Luoyu Road, Wuhan 430079, China

be generated simultaneously with real-time orbits, rather than through the traditional “two-step” method (Dai et al. 2022).

Although filter-based POD demonstrates several favorable properties, there are still factors that need to be considered and improved for practical applications. One limitation of filter-based POD is the slow convergence speed during the initialization or reconvergence period of the filter. This issue is particularly pronounced in the radial-track directions of GNSS satellites, where convergence takes the longest time due to the poor observation geometry. Qing et al. (2018) highlights the impact of prior constraints on initial orbit states on the convergence of BDS filter-based POD, showing that constraints based on broadcast ephemeris and ultra-rapid orbits can effectively reduce the time required to achieve decimeter-level accuracy. However, achieving centimeter-level accuracy still requires a much longer time due to the slow variations in ground GNSS observation geometry. Additionally, the massive GNSS network processing involved in filter-based POD is time-consuming due to the large number of estimated parameters (Gong et al. 2018). As a result, computational performance is another significant limitation of filter-based POD, potentially hindering its application in time-sensitive scenarios. Most recent research aimed at improving the computational efficiency of real-time GNSS network solutions focuses on parallel computing technologies, which require multi-core CPU resources (Zheng et al. 2024).

In addition to the efforts mentioned above, the utilization of LEO-onboard observations is another potential way to improve the performance of filter-based POD. It has been comprehensively demonstrated that LEO-onboard observations can significantly enhance the accuracy of post-processed integrated POD solutions, particularly when there is a limited number of ground stations or regional distributions. Zhu et al. (2004) were the first to integrate ground and LEO-onboard observations to determine the orbits of GPS, CHAMP, and GRACE satellites, with results indicating accuracy improvements for all satellites. Since LEO satellites serve as dynamic tracking stations in integrated POD solutions, the observation geometry of GNSS satellites, especially GEO satellites, can be significantly improved. Ge et al. (2017) validated the benefits of integrated POD for GEO satellites using simulated data, and Li et al. (2020) demonstrated improvements in the determination of BDS GEO satellites using onboard data from the Feng Yun-3 series satellites. Additionally, some studies further investigate specific influencing factors of integrated POD and the impact of LEO constellations (Li et al. 2019c).

From the above discussions, the slow convergence speed and heavy computational requirements of filter-based real-time POD still limit its availability. Although the utilization of LEO-onboard observations in previous studies demonstrates

its improvements for GNSS satellites, these studies still focus on the post-processed batch methods for GNSS POD. From the characteristics of LEO-onboard observations on observation geometry and enhancement on small-scale ground network, it is naturally expected that convergence time and computational performance of filter-based POD can be further enhanced by integrating LEO-onboard observations in real-time.

Therefore, in this study, we propose a real-time processing model that integrating LEO-onboard and ground observations with square root information filter (SRIF) to improve the performance of GNSS real-time orbits and clocks. For the first time, the LEO-onboard observations are applied to enhance the real-time filter-based estimation of GNSS orbits. Real data from LEO-onboard and ground observations are utilized to assess the improvements gained from incorporating LEO-onboard observations. Meanwhile, the impact of various factors on the effectiveness of LEO-onboard observations is systematically analyzed. The remainder of this study is organized as follows. Following this introduction, the methods used in the proposed model are presented. We then describe the real observation data and the specific processing strategies employed in the subsequent validation experiments. Next, the corresponding results and analysis of the proposed model are presented. Finally, we provide the conclusion of our study.

Methods

This section first describes the observation model of LEO-onboard and ground observations. Additionally, the basic orbit models of GNSS and LEO satellites used in our methods are introduced. Subsequently, the estimation method of real-time integrated orbit and clock determination is introduced in detail.

Basic observation and orbit model

In the field of precise orbit determination of GNSS and LEO satellites, the ionospheric-free (IF) combination of dual-frequency GNSS observations is commonly used to eliminate first-order ionospheric delays (Li et al. 2019a). Concretely, the linearized IF combined phase and code observation model for LEO-onboard and ground observations in the International Celestial Reference Frame (ICRF) can be expressed as follows:

$$\begin{aligned} p_{r,IF}^s &= \rho_r^s + u_r^s [\phi^s(T, TS_r^s) \Delta x_{orb}^s(T) - \Phi(TR_r) \Delta x_r - \bar{x}_r \delta_{erp} \Delta x_{erp}] \\ &\quad + cdt_r - cdt^s + M_r^s Z_r + d_{r,IF} - d_{IF}^s + e_{r,IF}^s \\ p_{leo,IF}^s &= \rho_{leo}^s + u_{leo}^s [\phi^s(T, TS_{leo}^s) \Delta x_{orb}^s(T) - \Delta x_{leo}] \\ &\quad + cdt_{leo} - cdt^s + d_{leo,IF} - d_{IF}^s + e_{leo,IF}^s \end{aligned} \quad (1)$$

$$\begin{aligned} l_{r,IF}^s &= \rho_r^s + u_r^s [\phi^s(T, TS_r^s) \Delta x_{orb}^s(T) - \Phi(TR_r) \Delta x_r - \bar{x}_r \delta_{erp} \Delta x_{erp}] \\ &\quad + cdt_r - cdt^s + M_r^s Z_r + \lambda_{IF} (N_{r,IF}^s + b_{r,IF} - b_{IF}^s) + \epsilon_{r,IF}^s \\ l_{leo,IF}^s &= \rho_{leo}^s + u_{leo}^s [\phi^s(T, TS_{leo}^s) \Delta x_{orb}^s(T) - \Delta x_{leo}] \\ &\quad + cdt_{leo} - cdt^s + \lambda_{IF} (N_{leo,IF}^s + b_{leo,IF} - b_{IF}^s) + \epsilon_{leo,IF}^s \end{aligned} \quad (2)$$

where the subscripts r , leo and s denote the ground station, LEO satellite and observed GNSS satellite, respectively; p and l denote the IF combined code and phase observations, respectively; ρ denotes the geometric distance calculated using the initial value of parameters; x_{leo} denotes the positions for leo ; x_r denotes the positions for r expressed in the Earth-Centered Earth-Fixed (ECEF) frame and \bar{x}_r denotes the initial value of x_r ; x_{orb}^s denotes the orbit state vector for the satellite s , including positions, velocities and solar radiation pressure (SRP) coefficients; x_{erp} denotes Earth rotation parameters (ERP), including x-pole, y-pole, UT1-UTC and excess length of day (LOD); $\Delta(*)$ denotes the corrections relative to the initial value of the corresponding parameter; TS and TR denote the signal transmission and reception time of the corresponding observation at the epoch T ; $\phi^s(T, TS)$ denotes the orbit state transition matrix from epoch T to TS ; $\Phi(TR)$ denotes the coordinate transformation matrix from ECEF to ICRF at the epoch TR ; δ_{erp} denotes the derivative of $\Phi(TR)$ w.r.t x_{erp} ; c is the speed of light; dt_r , dt_{leo} and dt^s denote the clock offset of r , leo and s , respectively; Z_r denotes the zenith troposphere wet delay (ZTD) of r and M_r^s denotes its mapping function; N denotes the carrier phase ambiguity in cycle and λ_{IF} is the wavelength of the IF combination; d denotes the code-specific hardware delay in meter; b denotes the phase-specific hardware delay in cycle; e and ϵ denote the unmodeled bias on code and phase observations, respectively.

Note that the caculation of p and l in Eqs. (1) and (2) requires the consideration of the precise bias models, including relativistic effects, phase wind up, tropospheric dry delays, tidal effects, phase center offsets (PCOs) and phase center variations (PCVs) (Saastamoinen 1972; Zumberge et al. 1997; Schaer et al. 2000; Kouba 2009; Luzum et al. 2012). In addition, in the multi-GNSS contexts, the inter-system bias (ISB) parameters should be estimated due to the difference of d between different navigation satellite systems (Zhang et al. 2016).

Generally, the initial values of the satellite orbit state vectors for the next epoch can be obtained from the integrated with the first-order differential equation of satellite motion:

$$\begin{bmatrix} \dot{x}^s \\ \dot{v}^s \\ \dot{x}_{leo} \\ \dot{v}_{leo} \end{bmatrix} = \begin{bmatrix} v^s \\ a^s \\ v_{leo} \\ a_{leo} \end{bmatrix} \quad (3)$$

where the x , v and a denote the position, velocity and acceleration of satellite. Also, the state-transition matrix ϕ can be computed by integrating from the orbit variational equation. Then the satellite orbit state transition equation can be expressed as follows:

$$\begin{cases} x_{orb}^s(T') \leftarrow x_{orb}^s(T) \\ x_{orb,leo}(T') \leftarrow x_{orb,leo}(T) \\ \Delta x_{orb}^s(T') = \phi^s(T, T') \Delta x_{orb}^s(T) + \omega^s(T, T') \\ \Delta x_{orb,leo}(T') = \phi_{leo}(T, T') \Delta x_{orb,leo}(T) + \omega_{leo}(T, T') \end{cases} \quad (4)$$

where $x_{orb,leo}$ denotes the satellite orbit vector for $r leo$, including positions, velocities, SRP coefficients, drag scale factors and empirical accelerations; T' denote the next epoch for T ; ω denotes the process noise; the other symbols have the same meaning in Eqs. (1) and (2). It is noticed that both $x_{orb,leo}$ and x_{orb}^s are estimated in the ICRF, which can avoiding the simplicifications in the modeling of Coriolis forces in the ECEF.

Real-time integrated precise GNSS orbit and clock estimation

Based on the above observation and orbit model, the estimated parameters X for real-time integrated precise GNSS orbit and clock estimation can be expressed as:

$$X = \left[x_{orb}^s, x_{orb,leo}, x_r, x_{erp}, \tilde{dt}^s, \tilde{dt}_r, \tilde{dt}_{leo}, Z_r, N_{r,IF}^s, N_{leo,IF}^s \right]$$

$$\begin{cases} \tilde{dt}^s = cdt^s + d_{IF}^s \\ \tilde{dt}_r = cdt_r + d_{r,IF} \\ \tilde{dt}_{leo} = cdt_{leo} + d_{leo,IF} \\ \tilde{N}_{r,IF}^s = \lambda_{IF} (N_{r,IF}^s + b_{r,IF} - b_{IF}^s) \\ N_{leo,IF}^s = \lambda_{IF} (N_{leo,IF}^s + b_{leo,IF} - b_{IF}^s) \end{cases} \quad (5)$$

where all symbols have the same meaning in the previous section. By simplifying the observation and orbit models into the following forms:

$$\begin{cases} X(T_i) = F(T_i)X(T_{i-1}) + w(T_i) \\ O(T_i) = H(T_i)X(T_{i-1}) + v(T_i) \end{cases} \quad i = 1, 2, \dots \quad (6)$$

where T_i denote the time of i th epoch; O denotes the measurement vector of GNSS observations; F and H denote the state transition matrix and observational design matrix, which can be established based on Eqs. (1), (2) and (4); w and v denote the process and measurement noise vector. Then the optimal estimation of $X(T_k)$ implies the minimization optimization problems as follows:

$$M(T_k) = \sum_{i=1}^k \left(\|w(T_i)\|_{\Lambda_w^{-1}(T_i)}^2 + \|v(T_i)\|_{\Lambda_v^{-1}(T_i)}^2 \right) + \|X(0) - X_{ini}\|_{\Lambda_{ini}^{-1}}^2$$

where Λ_v and Λ_w denote the variance matrix of v and w , respectively; X_{ini} denote the given priori initial values of the estimated state vector and Λ_{ini} denotes its variance. In our study, the real-time estimation of X is based on SRIF, which is often used in real-time massive GNSS network solutions such as POD and PCE due to its numerical stability (Dai et al. 2022; Zheng et al. 2024). Concretely, the flowchart of SRIF-based real-time integrated GNSS orbit and clock estimation is summarized in Fig. 1.

The priori GNSS satellite orbit state at first can be obtained from the broadcast ephemeris and the priori LEO satellite orbit state at first can be taken from standard single point positioning (SPP). Real-time preprocessing is carried out for new observations to eliminate gross errors and identify cycle slips (Blewitt 1990). To make sure the robustness of the filter results, the SRIF measurement update are performed along with a recursive detection, identification and adaptation (DIA) procedure (Teunissen 1990). In our proposed model, considering that the incorrect constraints introduced by ambiguity fixing errors are irreparable (Li et al. 2019b), the SRIF time update is carried out on the state vector with the ambiguity float solution. The traditional double-differenced (DD) AR strategy employed in the real-time AR. The estimated state vector with ambiguities fixed can be performed orbit integration and established the state transition equation. Particularly, the above data processing

flowchart can also be simplified and adapted for utilizing the LEO kinematic orbit model. In this case, the LEO orbit state vector consists of positions only and there is no need to consider the LEO satellites in the orbit integration procedure.

Data collection and processing strategy

To validate the proposed integrated processing model, we collected data from day of year (DOY) 210–216 of 2021, using real observation from 90 globally distributed Multi-GNSS Experiment (MGEX) ground stations and 8 LEO satellites (Montenbruck et al. 2017). These LEO satellites include Sentinel-3 A, Sentinel-3B, Sentinel-6 A, GRACE-C, GRACE-D, Swarm-A, Swarm-B, and Swarm-C. Although the MGEX stations and Sentinel-6 A can receive multi-GNSS observations, most LEO platforms capable of tracking multiple GNSS constellations do not have publicly available data at this time. Therefore, we focus on utilizing GPS-only observations in our study. Figure 2 illustrates the specific distribution of the ground networks of various sizes used in the subsequent experiments.

The ground and LEO-onboard observations are processed using the real-time model to simulate the generation of real-time GPS orbits and clocks. The specific observation and orbit models used in the real-time integrated processing are summarized in Table 1.

As for the configuration of the stochastic model, the GNSS satellite clocks, and both ground station and LEO-onboard receiver clocks are modeled with white noise. Ground station positions are strongly constrained using the recent IGS weekly solutions. Carrier phase ambiguities are estimated as the constant values throughout their observation period. Other parameters in the estimated state vector are modeled using a random walk model (Dai et al. 2019, 2022). Specially, the UT1 parameter of ERP is strongly constrained to the priori value comes from IERS Bulletin A. The specific empirical setting of model noise used in SRIF is summarized in Table 2. As for the noise for IF combined code and carrier phase observations, they are set to the 0.6m and 4mm, respectively, and they are multiplied by the following elevation-related factor when used (An et al. 2020):

$$\text{factor} = \begin{cases} 1 & E > 30^\circ \\ 1/\sin(E) & E \leq 30^\circ \end{cases} \quad (7)$$

which E is the elevation of the observation.

In the following experiments, we tested several different solutions to evaluate the performance of the proposed real-time integrated processing model. Abbreviations for all solutions and their corresponding descriptions are summarized in Table 3. These abbreviations are used in combination. Additionally, the symbols “D” and “K” are

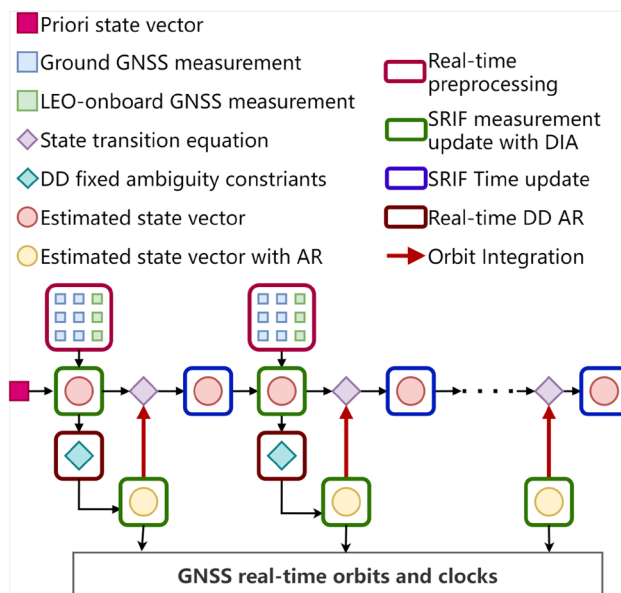


Fig. 1 Flowchart of the real-time GNSS orbit and clock estimation based on integrated processing of LEO-onboard and ground observations

Fig. 2 Distribution of various size ground network used in validation experiments

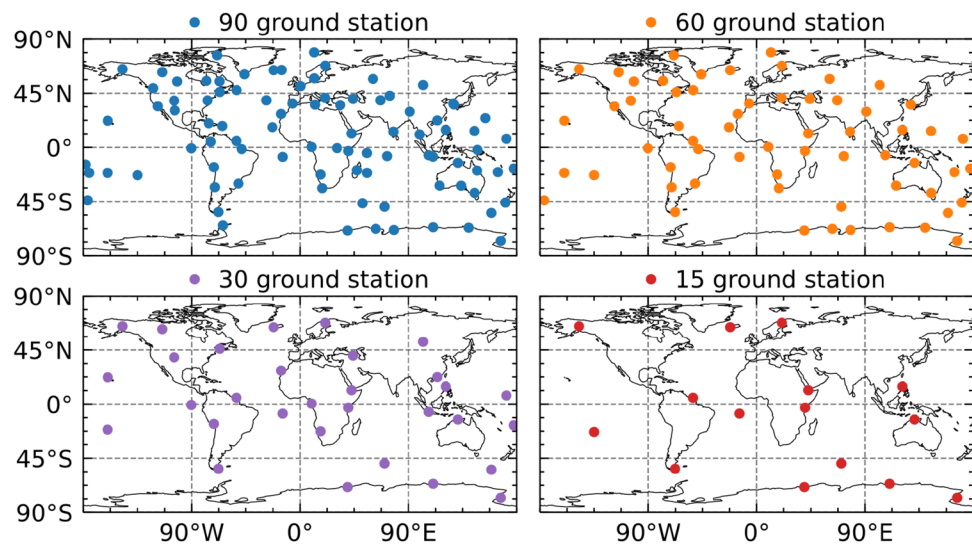


Table 1 Observation and orbit model applied in real-time integrated processing

Observation model	Applied model
Observations	Undifferenced IF combined GNSS code and carrier phase observations
Signal selection	GPS: L1 + L2
Sampling	30 s
Elevation cutoff	7° for ground stations 1° for LEO-onboard receiver
Relativistic effects	Corrected (Luzum and Petit 2012)
Phase windup	Corrected (Wu et al. 1993)
Tidal effects	Corrected for ground stations (Luzum and Petit 2012)
Tropospheric dry delay	Saastamoinen model for ground stations
Tropospheric mapping function	GMF mapping function for ground stations (Boehm et al. 2006)
Antenna phase center	Ground stations are corrected with IGS14 antenna file LEO satellites are corrected with the post-processed calibrated values
Orbit model	Applied model
Earth gravity	EIGEN-6S model (12 × 12) for GNSS satellites EIGEN-6S model (70 × 70) for LEO satellites (Förste et al. 2012)
Solar tide and pole tide	Solid earth pole: IERS conventions 2010 (Luzum and Petit 2012) Ocean tide: FES2014b (Lyard et al. 2021)
N-body gravity	Sun, moon, and planets; ephemeris provided from JPL DE405
SRP	GPS satellites: ECOM2 (Arnold et al. 2015) LEO satellites: Box-wing
Earth radiation	Considered (Rodriguez-Solano et al. 2012)
Antenna thrust	Considered (Steigenberger et al. 2018)
Atmospheric density	NRLMSISE00 only for LEO satellites (Picone et al. 2002)
Empirical acceleration	Considered only for LEO satellites (along-track and cross-track directions)

only used in the context of “G-L” solution. The term “AR” in “G-only” refers exclusively to “AR without LEOs”. In some experiments, the notation “G-NL” is used to indicate that “N” LEO satellites were included in the “G-L” solution.

Experimental results and analysis

We first evaluate the impact of integrating LEOs on the float and AR solution of real-time orbits and clocks from multiple perspectives, including the number of LEOs, the

Table 2 Empirical settings of model noise for parameters in filter

Item	Model noise per unit time (s^{-1})
Satellite positions	GPS: $1 \times 10^{-8} m$ LEO: $1 \times 10^{-6} m$
Satellite velocities	GPS: $1 \times 10^{-9} m/s$ LEO: $1 \times 10^{-7} m/s$
SRP coefficients	GPS: 1×10^{-8} LEO: 1×10^{-5}
Atmospheric drag factor	LEO: 1×10^{-5}
Empirical acceleration	LEO: $1 \times 10^{-6} m/s^2$
ERP	X-, Y-Pole: 1×10^{-7} arcsec
ZTD	0.25 mm

Table 3 Abbreviations and descriptions for each solution

Abbreviations	Description
G-only	Processing with ground stations only
G-L	Integrating ground and onboard observations
D/K	Using LEO reduced dynamic/kinematic orbit model in "G-L"
Float	Processing with ambiguity float mode
AR with/without LEOs	Real-time DD AR with/without consideration of LEO-based ambiguities

orbit models of LEOs, and the baselines between LEOs. Next, we analyze the performance of real-time integrated solutions across different ground networks. Finally, we validate the proposed model with real-time kinematic PPP.

Real-time integrated processing with different number of LEOs

The integrated processing solutions "G-L_K_float" and "G-L_D_float" were tested with varying numbers of LEO satellites. The eight LEO satellites were added to the experiments in the following order: Sentinel-6 A, Sentinel-3 A, Sentinel-3B, GRACE-C, GRACE-D, Swarm-B, Swarm-A, and Swarm-C. The ground observations used in the experiments in Sects. "Real-time integrated processing with different number of LEOs" and "Real-time integrated processing with AR" were all from the "30 ground stations" shown in Fig. 2. Figure 3 displays the orbit differences series between the real-time GPS orbits and the CODE final orbit products on DOY 210–212 in 2021. The orbit convergence criteria used in our study require that the orbit signal-in-space range errors (SISRE) remain within 5 cm for three consecutive hours (Montenbruck et al. 2018).

It was observed that, compared to ground-only solution "G-only_float", the integrated solutions using both LEO dynamic and kinematic model exhibit smaller orbit

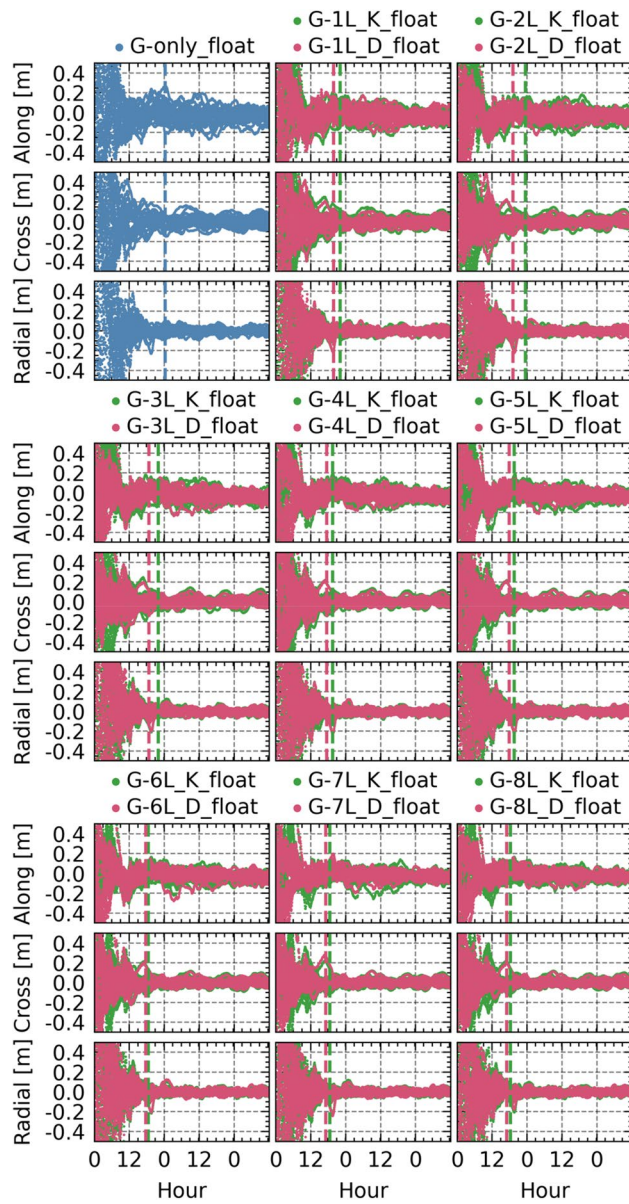


Fig. 3 Time series of GPS satellite orbit differences with respect to the CODE final products by comparing "G-only_float", "G-L_K_float" and "G-L_D_float" across various number of LEO satellites (The dashed line indicates the average convergence time of all satellites)

difference variations, particularly in the along-track and cross-track directions. This improvement is due to the significant enhancement in observation geometry provided by the addition of LEO satellites. Meanwhile, the integrated solutions resulted in shorter convergence times and the dynamic model of LEO satellites led to better overall results for the integrated processing model due to the stronger constraints. Additionally, the difference in convergence times between these two integrated solutions decreased as the number of LEO satellites increased.

The distribution of convergence times for each solution is shown in Fig. 4. The specific statistical results are presented in Table 4. For the ground-only solution, convergence generally takes more than a full day. In contrast, when using all 8 LEOs, the convergence times for the integrated solutions using LEO dynamic and kinematic model are 18.19 and 16.88 h, respectively. Additionally, the distribution of convergence times for the LEO dynamic model is more centralized compared to the kinematic model, with this difference being more pronounced when fewer LEOs are used. Compared to ground-only solution, the improvement in convergence time using integrated solutions with 1 to 8 LEOs ranges from 9.3 to 25.0% for the kinematic model and from 18.6 to 30.4% for the dynamic model. It is noticed that the degree of improvement is correlated with the LEO orbit diversity. Specifically, Sentinel-3 A/3B, GRACE-C/D, and Swarm-A/C have similar orbital types, and their contributions to the number of LEO-onboard observations result in only slight improvements in convergence.

In addition to the convergence analysis, we also evaluated the accuracy of real-time orbits and clocks for each solution. Figure 5 presents the RMS values of orbit differences in the along-track, cross-track, radial directions, and the standard deviation (STD) values of clock differences, as well as their improvements compared to the ground-only solution for the integrated solutions with different numbers of LEOs. Compared to ground-only solution, the improvements in orbit 3D RMS and clock STD values using the integrated solutions with 1 to 8 LEOs range from 9.7% to 35.8% and 8.3% to 35.4% for the kinematic model, and from 23.5 to 46.9% and from 5.4 to 37.5% for the dynamic model. Similar to the characteristics observed in the convergence analysis, the increase in the number of observations from LEOs with similar orbital types resulted in only marginal improvements in orbit and clock accuracy.

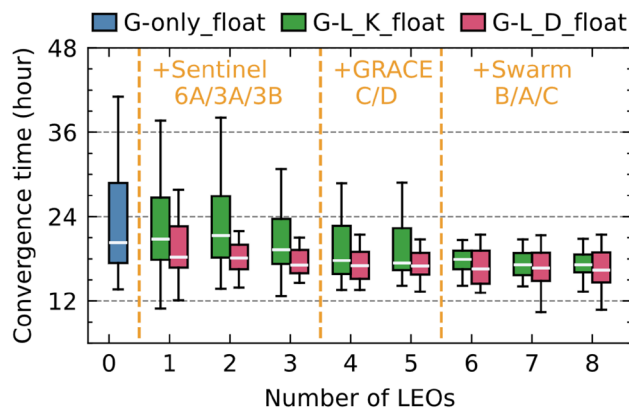


Fig. 4 Distribution of convergence time of GPS satellite by comparing “G-only_float”, “G-L_K_float” and “G-L_D_float” across various number of LEO satellites (The boxplot diagram shows the dataset’s minimum, maximum, median, and first and third quartiles)

Table 4 Average convergence time of GPS satellite by comparing “G-only_float”, “G-L_K_float” and “G-L_D_float” across various number of LEO satellites

The number of LEOs	Average convergence time (hour)		
0	24.26	G-L_K_float	G-L_D_float
1	22.00	19.75	
2	23.34	19.00	
3	21.91	18.71	
4	19.43	17.44	
5	19.43	17.71	
6	18.48	17.63	
7	18.47	17.09	
8	18.19	16.88	

Figure 6 further illustrates the specific improvements in orbits and clocks for each satellite. It should be noted that, to eliminate the systematic errors caused by the clock datum, we have aligned the clock time series to the reference satellite G08 in the clock comparison. Compared to ground-only

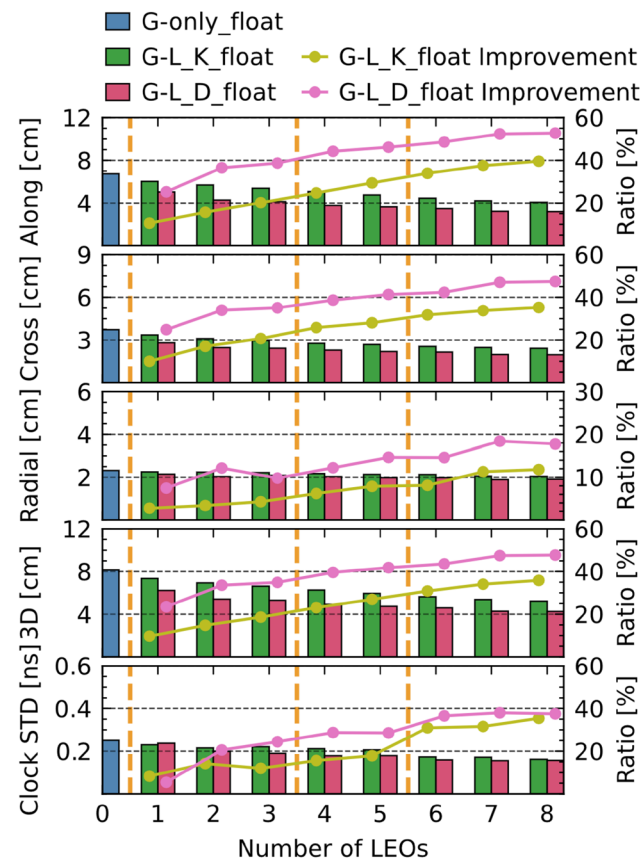
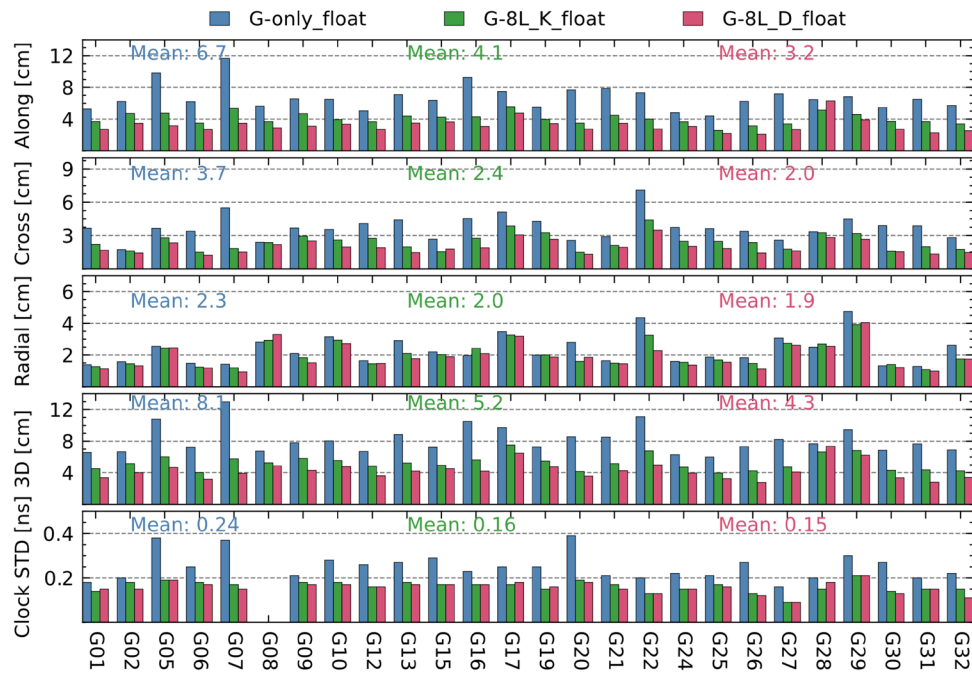


Fig. 5 RMS of GPS satellite orbit differences, STD of GPS satellite clock differences and their improvements by comparing “G-only_float”, “G-L_K_float” and “G-L_D_float”

Fig. 6 RMS of GPS satellite orbit differences and STD of GPS satellite clock differences by comparing “G-only_float”, “G-8L_K_float” and “G-8L_D_float”



solution, the integrated solution using the dynamic model improves the average 3D RMS for GPS satellite orbits by 46.9%, from 8.1 to 4.3 cm, and improves the average STD value for GPS satellite clocks by 37.5%, from 0.24 to 0.15 ns. Even when compared with using the kinematic model, the integrated solution using the dynamic model still significantly improves real-time orbit accuracy in the along-track and cross-track directions by 22.0% and 16.7%, respectively.

Real-time integrated processing with AR

In this section, we assess the real-time integrated POD with AR solutions. We also tested “AR without LEOs” and “AR with LEOs” to evaluate the impact of LEO-based double-difference (DD) ambiguity constraints on real-time integrated processing. For all solutions, integer ambiguity constraints were applied 24 h after the filter started to ensure basic filter convergence.

Table 5 presents the statistics of the fixing rate for DD narrow-lane (NL) ambiguities in each solution. Since wide-lane (WL) ambiguities can be derived from the Melbourne–Wübbena (MW) combination, their fixing primarily depends on the quality of GNSS observations. Therefore, our focus is on the fixing of narrow-lane (NL) ambiguities. As shown in Table 5, when using AR without consideration of LEO-based ambiguities, the average fixing rates for ground-only solution, the integrated solutions using the kinematic and dynamic model are 87.1%, 88.1%, and 88.2%, respectively, indicating that the addition of LEO-onboard observations has a marginal impact on ground-based DD ambiguity fixing. When using AR with consideration of

Table 5 Statistics on fixing rate of NL ambiguity by comparing “G-only”, “G-8L_K” and “G-8L_D” across different AR strategies

Strategy	Fixing rate (%)	
	Average	STD
G-only_AR	87.1	3.4
G-8L_K_AR without LEOs	88.1	3.3
G-8L_D_AR without LEOs	88.2	3.3
G-8L_K_AR with LEOs	82.9	4.0
G-8L_D_AR with LEOs	86.4	3.5

LEO-based ambiguities, the fixing rate of integrated solution using the dynamic model (86.4%) is higher than that (82.9%) of using kinematic model. However, the fixing rates for these two solutions are still lower than those solutions using AR without consideration of LEO-based ambiguities. This can be attributed to the shorter common-view time of LEO-based DD ambiguities, which leads to an overall lower fixing rate.

Figure 7 shows the RMS of orbit differences with respect to CODE final products in the along-track, cross-track, radial, and 3D directions by comparing the integrated solutions using 8 LEOs and ground-only solution. When using AR without LEO-based ambiguities, the average 3D RMS for ground-only solution, the integrated solutions with kinematic and reduced model is 6.2, 4.7, and 4.0 cm, respectively. Compared to their corresponding float solutions shown in Fig. 6, the improvements are 23.5%, 9.6%, and 7.0%, indicating that the benefits of using AR for integrated solutions are smaller than



Fig. 7 RMS of GPS satellite orbit differences by comparing “G-only”, “G-8L_K” and “G-8L_D” across different AR strategies

ground-only solution. This is reasonable because the contributions of both AR and LEO-onboard observations primarily enhance the along-track and cross-track components of GNSS satellite orbits (Dai et al. 2022). When further using AR with LEO-based ambiguities, the contributions to the integrated solutions with the kinematic and dynamic model both are marginal in the 3D direction. This is primarily due to the limited number of LEO-based DD ambiguities and their lower fixing rate.

We also assessed the orbit accuracy of LEO satellites by comparing them with post-processed products, as shown in Fig. 8. It should be noted that the orbit accuracy of LEOs is measured only after the GPS satellites have converged to ensure the absolute accuracy of the LEO satellites. The first noticeable observation from Fig. 8 is that using the dynamic model significantly improves the orbit accuracy of LEO satellites in the integrated solution. When applying AR with LEO-based ambiguities in the integrated solutions, the average 3D RMS improves to 7.7 cm for the kinematic model and 3.9 cm for the dynamic model, with improvements of 7.2% and 7.1%, respectively, compared to AR without LEO-based ambiguities. Considering that twin LEO satellites are more favorable for the construction and fixing of LEO-based DD ambiguities, GRACE-C shows substantial improvements in 3D RMS when comparing AR with and without LEO-based ambiguities, with improvements of 19.0% and 10.6% for the kinematic and dynamic models, respectively.

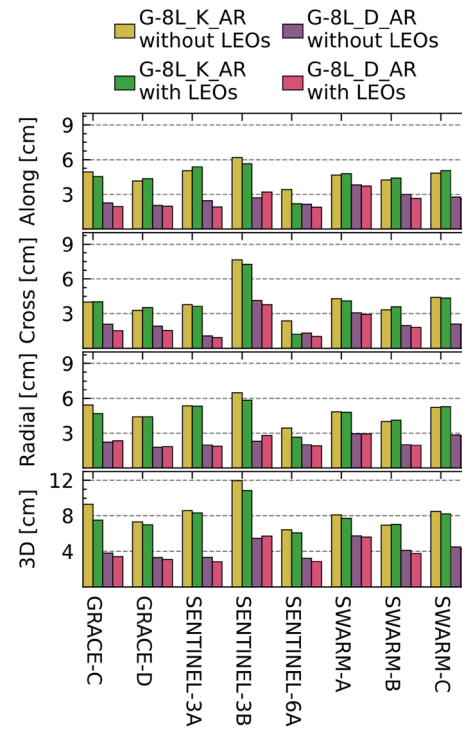


Fig. 8 RMS of LEO satellite orbit differences by comparing “G-8L_K” and “G-8L_D” across different AR strategies

Real-time integrated processing with different ground network

To analyze the performance of the integrated solutions with

different numbers of global stations, we performed each solution using the various ground networks shown in Fig. 2. The results of the 3D RMS of orbit differences are presented in Fig. 9. For the integrated solutions, the benefits of adding ground stations become less significant once the number of stations exceeds 30. Consequently, the integrated solutions using fewer ground stations can achieve comparable accuracy to ground-only solution with a denser ground network. Specifically, when without using AR, the accuracy of the integrated solutions with the dynamic model using 15 ground stations is significantly better than that of ground-only solution with 90 ground stations. Moreover, when further applying AR, the accuracy of integrated solutions with the dynamic model using 30 ground stations is comparable to that of ground-only solution with 90 ground stations. Therefore, the integrated solutions can significantly reduce the dependence on the number and distribution of ground stations for real-time GNSS POD.

We further assessed the computational efficiency of each solution using different ground networks, and the results for execution time per epoch are shown in Fig. 10. The computational time for all solutions increases rapidly with the number of stations. This is particularly evident in the solutions with AR, where more stations require real-time DD AR to be performed with additional DD baselines. Additionally, due to the extra orbit state parameters and transition equations for LEO satellites, the integrated solution with the dynamic model shows a faster growth trend in computational time compared to the ground-only solution and integrated solution with the kinematic model.

As mentioned earlier, the integrated solutions require fewer stations to achieve the same accuracy, resulting in higher computational efficiency. For example, to achieve an average 3D RMS of 4 cm for GPS satellites, the required

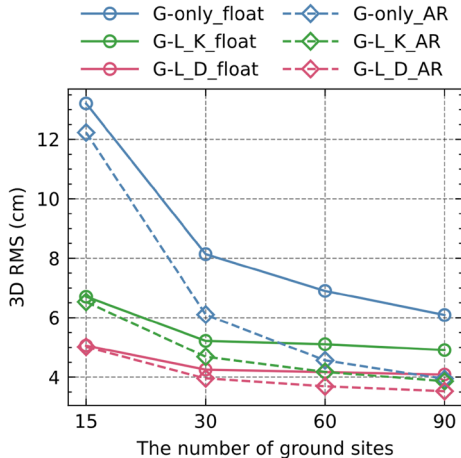


Fig. 9 RMS of GPS satellite 3D orbit differences by comparing “G-only”, “G-8L_K” and “G-8L_D” across various number of ground stations

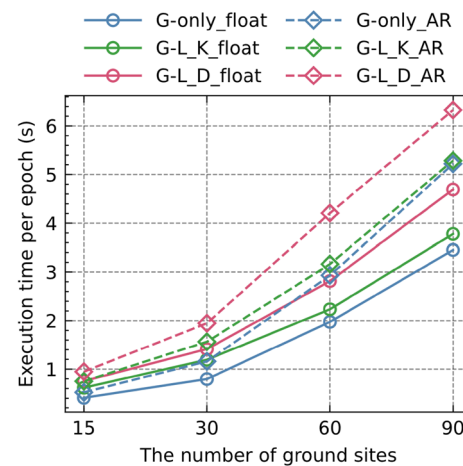


Fig. 10 Average execution time of per epoch by comparing “G-only”, “G-8L_K” and “G-8L_D” across various number of ground stations

number of stations is approximately 90 for ground-only solution, 60 for the integrated solution with the kinematic model, and 30 for the integrated solution with the dynamic model, as presented in Fig. 9. The corresponding numbers of observations and parameters, as well as the execution times, are shown in Fig. 11. For the integrated solution with dynamic model, the average number of observations and parameters are 620 and 918, representing reductions of 55.8% and 32.1%, respectively, compared to 1404 and 1352 for ground-only solution. The smaller reduction in parameters compared to observations is primarily due to the additional LEO orbit

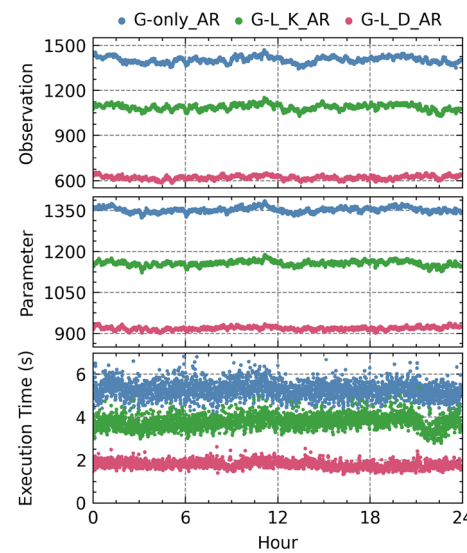


Fig. 11 Time series of number of observations (top), number of parameters (middle) and execution time (bottom) by comparing “G-only_AR”, “G-8L_K_AR” and “G-8L_D_AR” on DOY 211 of 2021

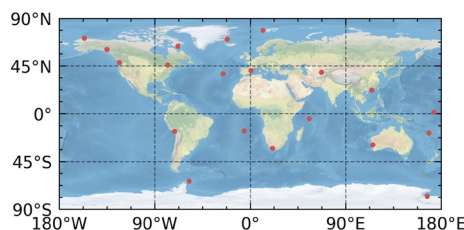


Fig. 12 Distribution of the stations used for real-time kinematic PPP validation

state parameters for the dynamic orbit model. Ultimately, the average computation time per epoch for the integrated solution with dynamic model is 66.0% shorter than for ground-only solution, reducing from 5.3 to 1.8 s.

Validation of real-time kinematic PPP

To further assess the real-time orbits and clocks produced by the real-time integrated processing strategies, we selected 20 globally distributed stations to perform real-time kinematic PPP, as shown in Fig. 12. Our focus is on comparing the ground-only solution “G-only_AR” using 30 sites with the integrated solution “G-L_D_AR” using 15 sites, as these

configurations have similar computational efficiency, with an execution time per epoch of about 1 s.

Figure 13 presents the time series of positioning errors from PPP float solutions using real-time products from ground-only solution and the integrated solution for five stations on DOY 211 of 2021. The PPP solutions based on the integrated solution show a slight improvement in the convergence of the East (E) and North (N) components for some stations compared to ground-only solution. However, more significant improvement is observed in overall positioning accuracy. For all five stations, when using the integrated solution, the positioning errors in all three components exhibit a lower magnitude of variation compared to ground-only solution.

The statistic of convergence time and positioning accuracy of 20 stations from DOY 211 to 216 of 2021 have been evaluated and the results are presented in Figs. 14 and 15. Here, the criterion for convergence of PPP is defined as the duration required for the horizontal positioning errors to below 5 cm for 10 consecutive epochs. The results of high accuracy but more time-consuming strategies “G-only_AR with 90 sites” and “G-L_D_AR with 30 sites” are also given for comparison. The convergence time of PPP solutions between each solution shows the marginal differences. The PPP solutions based on

Fig. 13 Positioning errors of five stations (KITG, NYAL, OHI3, SCOR and YARR), which derived from GPS PPP float solutions with products based on “G-only_AR with 30 sites” and “G-L_D_AR with 15 sites” on DOY 211 of 2021

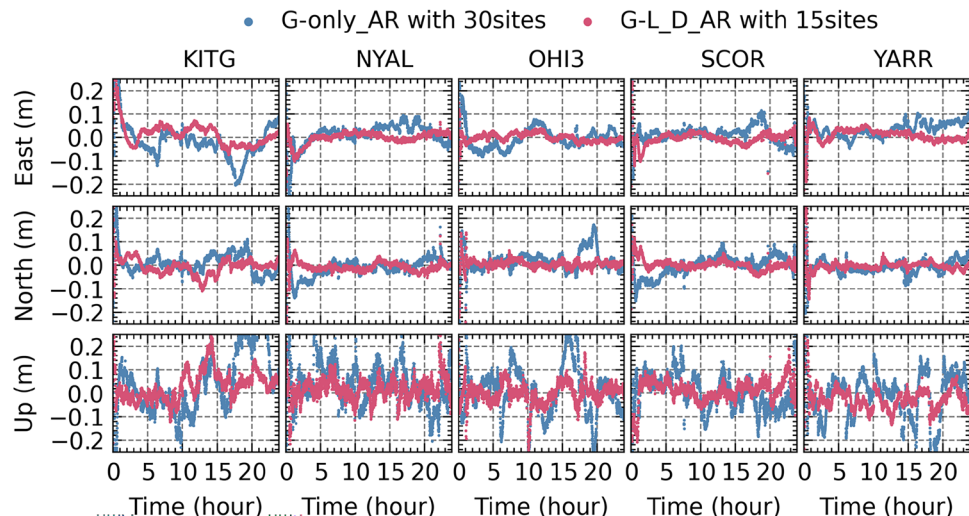


Fig. 14 Distribution of the convergence time of GPS PPP float solutions with products based on different strategies for all 20 stations from DOY 211 to 216 of 2021

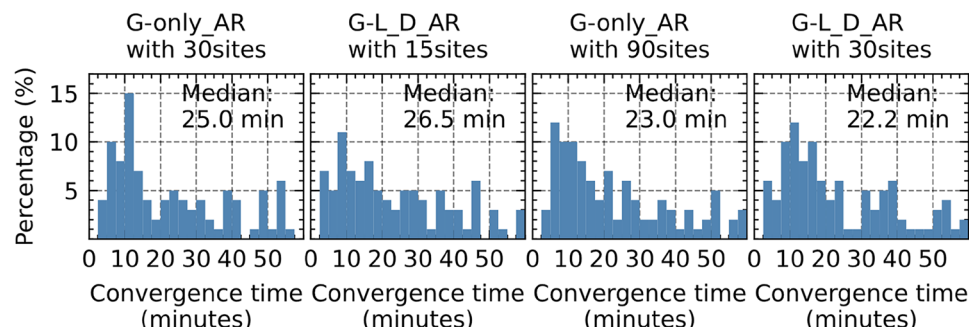
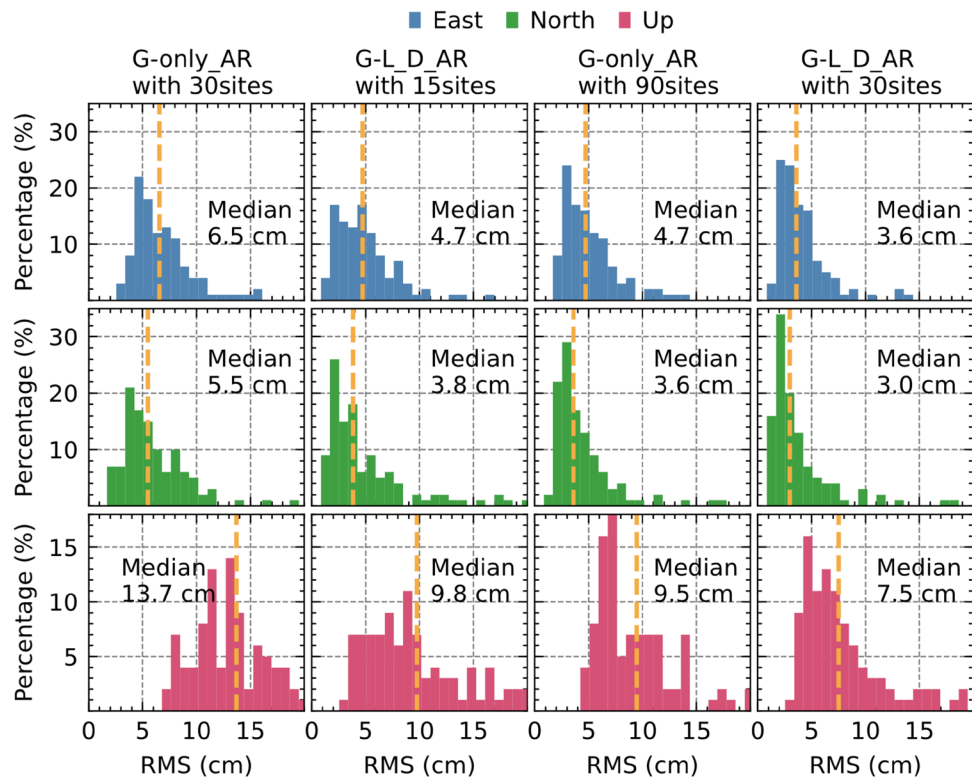


Fig. 15 Distribution of the positioning errors of GPS PPP float solutions with products based on different strategies in east, north and up components for all 20 stations from DOY 211 to 216 of 2021



“G-L_D_AR with 30 sites” show the best convergence performance, which its median value is 22.2 min. As for positioning accuracy, when using efficient products of “G-L_D_AR with 15 sites”, the positioning accuracy of PPP solutions based on the integrated solution can be improved 27.7% in the E component (from 6.5 to 4.7 cm), 30.9% in the N component (from 5.5 to 3.8 cm) and 28.5% in the U component (from 13.7 to 9.8 cm), when compared to that of “G-only_AR using 30 sites”. The positioning accuracy based on this efficient products is even close to that based on high accuracy ground-only solution “G-only_AR with 90 sites”. This indicates the integrated solution can significantly improve the products accuracy while meeting the timing requirements of highly time-sensitive cases. When using the products of “G-L_D_AR with 30 sites”, the positioning accuracy of PPP solutions is significantly better than other solution. Moreover, as shown in Fig. 10, the computational time of “G-L_D_AR with 30 sites” is still substantially smaller than that of “G-only_AR with 90 sites”. In summary, all results demonstrate the advantage of the proposed model in balancing efficiency and accuracy for real-time GNSS precise orbit and clock estimation.

Conclusions

In this study, we propose a real-time integrated processing LEO-onboard and ground observations model to improve the GNSS real-time orbits and clocks. The performance

of real-time integrated POD is investigated from multiple aspects and the real observation data from eight LEO satellites and globally distributed MGEX stations covering DOY 210 to 216 of 2021 are collected for performing validation experiments.

To validate the integrated solution, the convergence time, orbits and clocks accuracy of GPS satellites using different number of LEOs are analyzed. Compared to traditional ground-only solution, the improvement in convergence time using the integrated solution for the kinematic and dynamic model increase from 9.3 to 25.0% and from 18.6 to 30.4% with the addition of one to eight LEO satellites, respectively. As for 3D RMS of orbits and average STD of clocks, by employing the integrated solution with the dynamic model and eight LEO satellites, they can be significantly improved by 46.9% (from 8.1 to 4.3 cm) and 37.5% (from 0.24 to 0.15 ns), respectively. We further assess the performance of real-time integrated POD with different AR strategies. By using the integrated solution and AR without LEO-based ambiguities, the average improvements on orbit 3D RMS are 14.8 and 27.8% for the kinematic and dynamic model when compared to ground-only solution, respectively. As for further considering LEO-based ambiguities in AR, the improvement on GPS satellite orbits is marginal on 3D directions.

The impact of different number of ground stations on real-time integrated POD is also investigated. The results indicate that the dependence of real-time POD on massive dense ground network can be significantly reduced with

the addition of LEO-onboard observations. As a result, the real-time integrated processing solution can improve computational efficiency by about 66% without loss of precision. The real-time kinematic PPP are also performed for testing real-time orbits and clocks based on traditional strategy and the proposed integrated model which have close computational time. The positioning accuracy of GPS PPP float solutions with the proposed model is 4.7 cm, 3.8 cm and 9.8 cm in the east, north and up components, respectively, with improvements of 27.7, 30.9 and 28.5% compared to the solutions with the traditional strategy.

In conclusion, the characteristic of the proposed integrated processing model indicates the better real-time GNSS products accuracy and efficiency in a highly time-sensitive scenarios. As the gradual construction of the large LEO constellations, it is expected to see further improvements in GNSS real-time orbits and clocks from real-time integrated processing model.

Acknowledgements This study is financially supported by the National Natural Science Foundation of China (Grant No. 42425401, 42304019, 42388102), China Postdoctoral Science Foundation (Grant No. 2023M732687), and China National Postdoctoral Program for Innovative Talents (Grant No. BX20230274). The algorithm implementation is based on the GNSS+ REsearch, Application and Teaching (GREAT) software developed by the GREAT Group, School of Geodesy and Geomatics, Wuhan University. The numerical calculations in this paper were done on the supercomputing system in the Supercomputing Center of Wuhan University.

Author's contribution All authors contributed to the study conception and design. Material preparation, data collection and analysis were performed by HZ and YY. The first draft of the manuscript was written by HZ and all authors commented on previous versions of the manuscript. All authors read and approved the final manuscript.

Data availability The GNSS observations from ground stations are available in Crustal Dynamics Data Information System, <https://cds.nerc.ac.uk/>. The CODE final orbit and clock products are available in the IGS repository, <ftp://igs.gnsswhu.cn/pub/gps/products/mgex/>. The LEO onboard observations can be downloaded from <ftp://isdcftp.gfz-potsdam.de/>.

Declarations

Conflict of interest The authors declare no competing interests.

References

- Arnold D, Meindl M, Beutler G, Dach R, Schaefer S, Lutz S, Prange L, Sośnicka K, Mervart L, Jäggi A (2015) CODE's new solar radiation pressure model for GNSS orbit determination. *J Geodesy* 89(8):775–791. <https://doi.org/10.1007/s00190-015-0814-4>
- An X, Meng X, Jiang W (2020) Multi-constellation GNSS precise point positioning with multi-frequency raw observations and dual-frequency observations of ionospheric-free linear combination. *Satellite Navig* 1(1):7. <https://doi.org/10.1186/s43020-020-0009-x>
- Blewitt G (1990) An automatic editing algorithm for GPS data. *Geophys Res Lett* 17(3):199–202. <https://doi.org/10.1029/GL017i003p00199>
- Boehm J, Niell A, Tregoning P, Schuh H (2006) Global Mapping Function (GMF): A new empirical mapping function based on numerical weather model data. *Geophys Res Lett*. <https://doi.org/10.1029/2005GL025546>
- Dai X, Gong X, Li C, Qing Y, Gu S, Lou Y (2022) Real-time precise orbit and clock estimation of multi-GNSS satellites with undifferenced ambiguity resolution. *J Geodesy* 96(10):73. <https://doi.org/10.1007/s00190-022-01664-3>
- Dai X, Lou Y, Dai Z, Qing Y, Li M, Shi C (2019) Real-time precise orbit determination for BDS satellites using the square root information filter. *GPS Solut* 23(2):45. <https://doi.org/10.1007/s10291-019-0827-1>
- Förste C, Bruinsma S, Shakoor R, Abrikosov O, Flechtner F, Marty J-C, Lemoine J-M, Dahle C, Neumeyer H, Barthelmes F et al (2012) A new release of EIGEN-6: The latest combined global gravity field model including LAGEOS, GRACE and GOCE data from the collaboration of GFZ Potsdam and GRGS Toulouse. *Egu General Assembly Conference Abstracts*, 2821
- Ge H, Li B, Ge M, Shen Y, Nie L, Schuh H (2017) Combined Precise Orbit Determination for High-, Medium-, and Low-Orbit Navigation Satellites. In Sun J, Liu J, Yang Y, Fan S, & Yu W (Eds), *China Satellite Navigation Conference (CSNC) 2017 Proceedings: Volume III* (Vol 439, pp 165–180). Springer Singapore. https://doi.org/10.1007/978-981-10-4594-3_15
- Gong X, Gu S, Lou Y, Zheng F, Ge M, Liu J (2018) An efficient solution of real-time data processing for multi-GNSS network. *J Geodesy* 92(7):797–809. <https://doi.org/10.1007/s00190-017-1095-x>
- Kouba J (2009) A guide to using International GNSS Service (IGS) products
- Li X, Chen X, Ge M, Schuh H (2019a) Improving multi-GNSS ultra-rapid orbit determination for real-time precise point positioning. *J Geodesy* 93(1):45–64. <https://doi.org/10.1007/s00190-018-1138-y>
- Li Z, Li M, Shi C, Fan L, Liu Y, Song W, Tang W, Zou X (2019b) Impact of ambiguity resolution with sequential constraints on real-time precise GPS satellite orbit determination. *GPS Solut* 23(3):85. <https://doi.org/10.1007/s10291-019-0878-3>
- Li X, Zhang K, Ma F, Zhang W, Zhang Q, Qin Y, Zhang H, Meng Y, Bian L (2019c) Integrated precise orbit determination of multi-GNSS and large LEO constellations. *Remote Sens* 11(21):2514. <https://doi.org/10.3390/rs11212514>
- Li X, Zhang K, Meng X, Zhang Q, Zhang W, Li X, Yuan Y (2020) LEO–BDS–GPS integrated precise orbit modeling using Feng-Yun-3D, Feng Yun-3C onboard and ground observations. *GPS Solut* 24(2):48. <https://doi.org/10.1007/s10291-020-0962-8>
- Luzum B, Petit G (2012) The IERS Conventions (2010): reference systems and new models. *Proc Int Astron Union* 10(H16):227–228. <https://doi.org/10.1017/S1743921314005535>
- Lyard FH, Allain DJ, Cancet M, Carrère L, Picot N (2021) FES2014 global ocean tide atlas: design and performance. *Ocean Sci* 17(3):615–649. <https://doi.org/10.5194/os-17-615-2021>
- Montenbruck O, Steigenberger P, Prange L, Deng Z, Zhao Q, Perosanz F, Romero I, Noll C, Stürze A, Weber G, Schmid R, MacLeod K, Schaefer S (2017) The multi-GNSS Experiment (MGEX) of the international GNSS service (IGS) – achievements, prospects and challenges. *Adv Space Res* 59(7):1671–1697. <https://doi.org/10.1016/j.asr.2017.01.011>
- Montenbruck O, Steigenberger P, Hauschild A (2018) Multi-GNSS signal-in-space range error assessment – methodology and results. *Adv Space Res* 61(12):3020–3038. <https://doi.org/10.1016/j.asr.2018.03.041>
- Picone JM, Hedin AE, Drob DP, Aikin AC (2002) NRLMSISE-00 empirical model of the atmosphere: statistical comparisons and

- scientific issues. *J Geophys Res: Space Phys.* <https://doi.org/10.1029/2002JA009430>
- Qing Y, Lou Y, Liu Y, Dai X, Cai Y (2018) Impact of the initial state on BDS real-time orbit determination filter convergence. *Remote Sens* 10(1):111. <https://doi.org/10.3390/rs10010111>
- Rodriguez-Solano CJ, Hugentobler U, Steigenberger P, Lutz S (2012) Impact of Earth radiation pressure on GPS position estimates. *J Geodesy* 86(5):309–317. <https://doi.org/10.1007/s00190-011-0517-4>
- Saastamoinen J (1972) Contributions to the theory of atmospheric refraction. *Bull Géodésique* 105(1):279–298. <https://doi.org/10.1007/BF02521844>
- Schaer S, Beutler G, Rothacher M, Brockmann E, Wiget A, Wild U (2000) The impact of the atmosphere and other systematic errors on permanent GPS networks. *Geodesy Beyond 2000: The Challenges of the First Decade IAG General Assembly Birmingham, Jul 19–30, 1999*, pp 373–380. https://doi.org/10.1007/978-3-642-59742-8_61
- Steigenberger P, Thoelert S, Montenbruck O (2018) GNSS satellite transmit power and its impact on orbit determination. *J Geodesy* 92(6):609–624. <https://doi.org/10.1007/s00190-017-1082-2>
- Teunissen PJG (1990) Quality control in integrated navigation systems. *IEEE Aerosp Electron Syst Mag* 5(7):35–41. <https://doi.org/10.1109/62.134219>
- Wu J-T, Wu SC, Hajj GA, Bertiger WI, Lichten SM (1993) Effects of antenna orientation on GPS carrier phase. *Manuscr. Geod.* 18:91–98. <https://doi.org/10.1007/BF03655303>
- Zhang W, Lou Y, Gu S, Shi C, Haase JS, Liu J (2016) Joint estimation of GPS/BDS real-time clocks and initial results. *GPS Solut* 20:665–676. <https://doi.org/10.1007/s10291-015-0476-y>
- Zheng H, Li X, Yuan Y, Wu J, Huang S (2024) An efficient parallel approach for quad-constellation GNSS real-time precise orbit determination enabling 5-second intervals updating. *Measurement* 233:114782. <https://doi.org/10.1016/j.measurement.2024.114782>
- Zhu S, Reigber C, König R (2004) Integrated adjustment of CHAMP, GRACE, and GPS data. *J Geodesy*. <https://doi.org/10.1007/s00190-004-0379-0>
- Zumberge JF, Heflin MB, Jefferson DC, Watkins MM, Webb FH (1997) Precise point positioning for the efficient and robust analysis of GPS data from large networks. *J Geophys Res: Solid Earth* 102(B3):5005–5017. <https://doi.org/10.1029/96JB03860>

Publisher's Note Springer Nature remains neutral with regard to jurisdictional claims in published maps and institutional affiliations.

Springer Nature or its licensor (e.g. a society or other partner) holds exclusive rights to this article under a publishing agreement with the author(s) or other rightsholder(s); author self-archiving of the accepted manuscript version of this article is solely governed by the terms of such publishing agreement and applicable law.